Lei *et al. Journal of Nanobiotechnology* (2025) 23:254
https://doi.org/10.1186/s12951-025-03329-7

Journal of Nanobiotechnology

RESEARCH Open Access

Dual-pathway tumor radiosensitization strategy based on engineered bacteria capable of targeted delivery of AuNPs and specific hypoxia alleviation

Lingling Lei[1,2,3†], Haonan Xu[1,3,4†], Mingjie Li[1,2,3], Meng Du[1,2,3*] and Zhiyi Chen[1,2,3*]

Abstract

Background Radiotherapy efficacy remains constrained by two key challenges: dose-dependent toxicity to healthy tissues at high radiation doses and hypoxia-mediated tumor radioresistance. While radiosensitizers like gold nanoparticles can enhance tumor-specific radiation deposition, their targeted delivery to tumors presents a significant hurdle. Bacteria have emerged as promising bio-carriers that not only actively target tumors and penetrate complex microenvironments, but can also be genetically engineered as multifunctional platforms for radiosensitizer delivery and hypoxia alleviation.

Results An integrated nanosystem (PCM@AuNPs), composed of engineered bacteria (PCM) and gold nanoparticles (AuNPs), is used to increase the effectiveness of radiotherapy. PCM can target and colonize tumor sites more effectively, thus improving the delivery efficiency of radiosensitizers. Furthermore, PCM overexpresses catalase (CAT), which decomposes excess H_2O_2 into O_2, helping to mitigate hypoxia in the TME. Under X-ray irradiation, PCM@AuNPs significantly enhance radiosensitization, leading to improved tumor growth inhibition while maintaining good biocompatibility.

Conclusions An effective strategy based on an integrated nanosystem (PCM@AuNPs) for radiosensitization through multiple pathways is developed. This novel engineered bacterial strategy holds great promise for enhancing radiosensitization in cancer therapy.

Keywords Hypoxia alleviation, Radiosensitization, Engineered bacteria, Catalase, Gold nanoparticle

†Lingling Lei and Haonan Xu contributed equally to this work and share the first authorship.

*Correspondence:
Meng Du
dumeng_work@126.com
Zhiyi Chen
zhiyi_chen@usc.edu.cn
[1]Key Laboratory of Medical Imaging Precision Theranostics and Radiation Protection, College of Hunan Province, Hengyang Medical School, The Affiliated Changsha Central Hospital, University of South China, Changsha, China
[2]Department of Medical Imaging, Hengyang Medical School, The Affiliated Changsha Central Hospital, University of South China, Changsha, China
[3]Institute of Medical Imaging, Hengyang Medical School, University of South China, Hengyang, China
[4]School of Public Health, University of South China, Hengyang, China

Introduction

Radiotherapy (RT) is a critical and integral component of comprehensive cancer treatment, with more than 50% of patients receiving it for either curative or palliative purposes [1, 2]. RT employs high-energy ionizing radiation to directly damage DNA and generate reactive oxygen species (ROS) through the radiolysis of water molecules, leading to apoptotic and necrotic cell death [3]. However, the efficacy of RT is significantly limited by the hypoxic environment within tumors which contributes to radioresistance and the toxicity associated with high-dose radiation to surrounding healthy tissues [4–6]. The introduction of radiosensitizers—molecules or materials capable of increasing radiation deposition and enhancing the radiosensitivity of tumor cells—can specifically address radioresistance and mitigate off-target toxicity [7].

Various radiosensitizers have been developed and applied in clinical treatments, such as cetuximab, paclitaxel, docetaxel [8]. However, physical toxicity and severe side effects generated by these drugs cannot be tolerated by patients during the RT [9]. Metal-based radiosensitizers, including platinum complexes, hafnium oxide nanoparticles, and gold nanoparticles (AuNPs) hold promising prospects, enhancing radiotherapy efficacy by localized radiation energy deposition. Platinum-based agents such as cisplatin primarily suppress DNA repair pathways, but their clinical utility is constrained by acquired resistance. Hafnium oxide nanoparticles, while effective in physical dose enhancement through high-Z element-mediated secondary electron emission, face challenges in tumor penetration due to their large hydrodynamic diameters [10]. In contrast, good biocompatibility and facile size controlling of AuNPs make it possible for an ideal radiosensitizer [11]. However, the dense extracellular matrix and abnormal blood vessel structures within tumors impede deep penetration of nanoparticles, especially in the core regions where optimal treatment is essential [12, 13]. Additionally, concerns regarding accumulation in other tissues and organelles persist, which could lead to severe side effects [14, 15]. Thus, enhancing the delivery efficiency of gold nanoparticles and achieving deep tissue penetration is crucial for effective RT sensitization in vivo. In recent years, bacteria-based therapeutic strategies have garnered significant attention for their potential to actively target tumors, and penetrate complex tumor microenvironments [16]. Thus, there is increased therapeutic specificity and efficacy in cancer treatment.

Integrating nanomaterials with bacteria allows for efficient drug delivery and deep tumor penetration [17–18]. Researchers have employed bacteria to deliver sonosensitizers [12], photosensitizers [19], and radiosensitizer nanoparticles [20]. Radiosensitizer accumulation in tumors can be enhanced by active bacterial delivery, enhancing tumor-specific radiation deposition. However, hypoxic tumor microenvironment limits ROS production [21–22]. Given the instability of strategies relying on external oxygen delivery, delivering enzymes such as catalase (CAT) has been explored to generate oxygen in situ by decomposing tumor-overexpressed H_2O_2 [23–25]. To overcome the rapid biodegradation of functional proteins in vivo, engineered bacteria have been utilized as localized "biofactories" to express therapeutic proteins within tumors [20]. However, constitutive overexpression of CAT imposes a significant metabolic burden on bacterial viability, hampering the treatment efficiency [26]. Ultrasound, as a noninvasive, safe, and deep tissue-penetrating technique, enables spatiotemporal control of thermal gradients through phase-array focused wavefronts, which orchestrate thermosensitive promoter-driven protein expression specifically within irradiated tumor regions [27, 28].

In our preliminary studies, we confirmed that ultrasound effectively controls the expression of interferon-γ in genetically engineered bacteria, enhancing the spatiotemporal control of protein expression and demonstrating promising therapeutic efficacy in tumor treatment [28]. Herein, we developed an integrated nanosystem (PCM@AuNPs) that combines engineered bacteria (PCMs) with AuNPs to increase sensitization to RT. The PCM component is designed to specifically target and colonize tumor sites, thereby improving the delivery efficiency of radiosensitizers. This increases radiation deposition and enhances DNA damage within the tumor. Additionally, PCM overexpresses CAT in response to ultrasound irradiation, which decomposes excess H_2O_2 into O_2, alleviating tumor hypoxia. When exposed to X-ray irradiation, the PCM@AuNPs system significantly enhances the radiosensitization effect, leading to improved tumor growth inhibition through multiple pathways while maintaining excellent biocompatibility. This innovative strategy, which uses engineered bacteria, holds significant therapeutic potential for enhancing radiosensitization (Fig. 1).

Methods

Materials

A 1,1-dioctadecyl-3,3,3,3-tetramethylindotricarbocyanine iodide (DiR) and a DNA damage detection kit were obtained from Beyotime Biotechnology (China). 1-Ethyl-3-(3-(dimethylamino)propyl) carbodiimide (EDC) and n-hydroxysuccinimide (sulfo-NHS) were purchased from Sigma (USA). Agar and LB broth were purchased from HuanKai Microbial (China). AuNPs were obtained from Shanghai Dibai Biotechnology Co., Ltd. (China). Dulbecco's modified Eagle's medium (DMEM), fetal bovine serum (FBS), penicillin, streptomycin solution, and

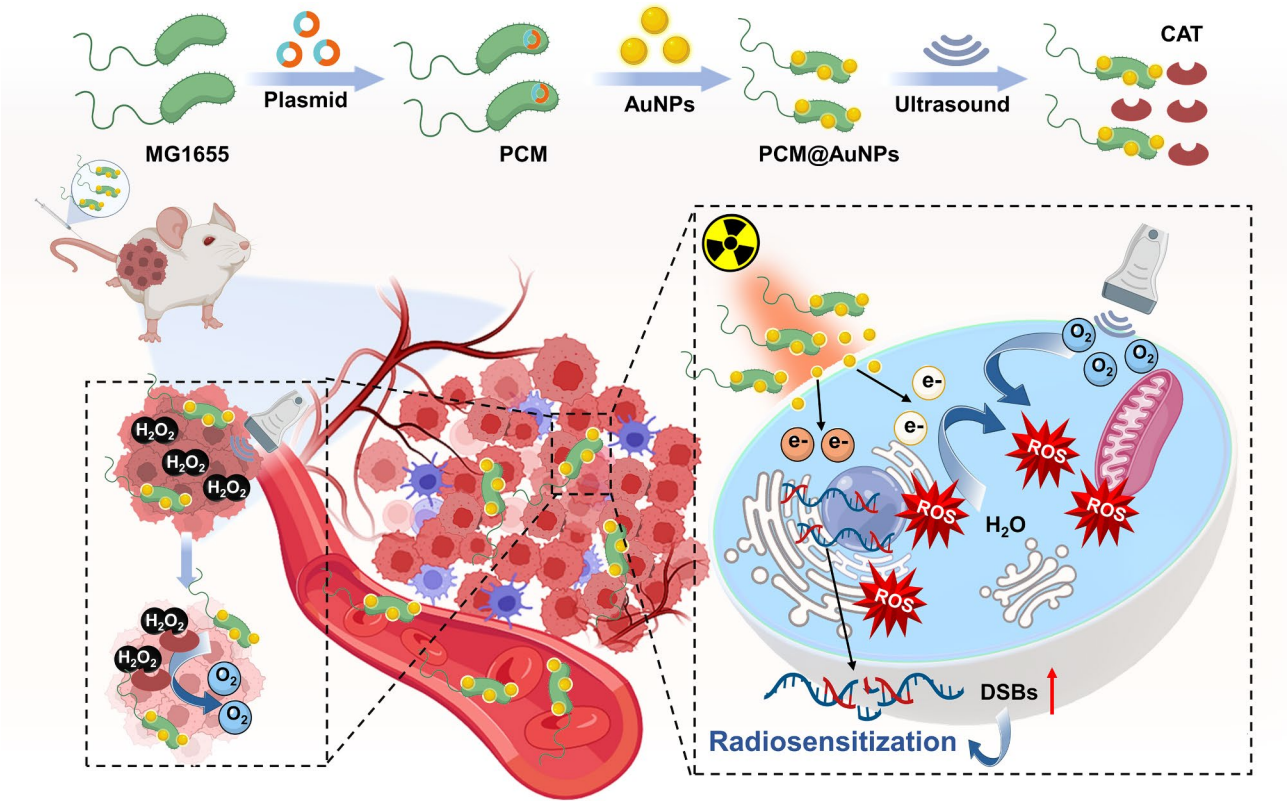

Fig. 1 Schematic illustration. Preparation steps of PCM@AuNPs. The ability of PCM to actively target tumors enables highly efficient delivery of gold nanoparticles (AuNPs) to tumors. After colonizing the tumor site, the PCM@AuNPs expressed a large amount of CAT upon ultrasound irradiation, which decomposed excessive H_2O_2 in the tumor, thereby increasing the oxygen concentration within the tumor. During radiation exposure, the gold nanoparticles in the tumor tissue absorb more radiation energy. An increase in the oxygen concentration enhances the generation of ROS, which, through a dual pathway, leads to greater DNA damage, thus achieving effective radiosensitization

trypsin containing 0.25% EDTA were purchased from Gibco (USA).

Cell lines

4T1 cells (mouse breast cancer cells) were obtained from the China Center for Type Culture Collection (CCTCC). The 4T1 cells were incubated in high-glucose DMEM containing 10% FBS and 1% penicillin–streptomycin in a humidified incubator with 5% CO_2 at 37 °C.

CAT plasmid and preparation of PCM

The *E. coli* MG1655 strain was purchased from Angyubio Biotechnology Co. (China). LB broth supplemented with 0.01% ampicillin was used for bacterial culture. The CAT-expressing thermosensitive plasmid (pBV220-CAT) synthesized by Sangon Biotech (China) contains the PR-PL tandem promoter and AmpR promoter. The recombinant plasmid was transformed into *E. coli* DH5α competent cells via a chemical transformation protocol. The pBV220-CAT plasmids were subsequently transformed chemically into the *E. coli* MG1655 strain to obtain PCM. The resulting PCM solution was plated on an LB solid plate with ampicillin and incubated at 37 °C for 12 h. PCM colonies were removed and amplified in LB medium at 37 °C and 220 rpm overnight. Afterward, the PCM solution was diluted 100-fold in LB medium and further grown to OD_{600} = 0.4–0.6 for further experiments.

Thermal-induced and ultrasound-induced CAT expression

The PCM transformed with the pBV220-CAT plasmid was incubated at 37–45 °C for a given time and further incubated for 2 hours at 37 °C. The bacterial OD was measured via a spectrophotometer. An equal number of 2×10^9 bacteria were collected, and the protein expression of CAT was analyzed via SDS-PAGE. To evaluate the feasibility of ultrasound-induced CAT gene expression, PCM was added to a 24-well plate (1000 μl per well). Ultrasound irradiation was applied at varying acoustic intensities of 0.8 W/cm^2, 1.2 W/cm^2, 1.6 W/cm^2, 2.0 W/cm^2, and 2.4 W/cm^2 with different durations to generate localized heat for gene induction, the selection of intensity referenced the work of Liu et al. [29] The fixed setting of intensity by Sonovitro ensured stability during sonication. Following the methodology of Chen et al. [28], an ON-OFF pulsed irradiation protocol was implemented to maintain consistent thermal conditions (ΔT within

± 1.0 °C over 30 min). The temperature of the PCM solution was monitored by an infrared thermal imager. In the following in vitro and in vivo experiments, we used this parameter (1.6 W/cm^2, 1 MHz, 3 s ON, and 7 s OFF), which could keep the irradiated bacterial mixture at 45 °C constant. Following ultrasound irradiation, western blotting was used to confirm CAT expression in vitro.

Preparation and characterization of PCM@AuNPs

The PCM was cultured to an OD_{600} of 0.4–0.6 at 37 °C, collected by centrifugation (3,000 rpm, 6 min), and then suspended in PBS. The AuNPs with -COOH surface modifications were suspended in 2 mL of MES buffer (0.1 M, pH = 5.5), and EDC and sulfo-NHS were added, corresponding to an EDC: sulfo-NHS: -COOH molar ratio of 30:30:1. After incubation at room temperature for 1 h to activate the carboxyl groups of COOH-AuNPs, the COOH-AuNPs were centrifuged at 10,000 rpm for 5 min and washed with PBS to remove residual EDC and sulfo-NHS. The centrifuged precipitate was washed 3 times, added to the PCM solution, and incubated for 2 h to obtain PCM@AuNPs. After centrifugation (3,000 rpm, 6 min), the PCM@AuNPs were suspended in PBS (pH = 7.4) and stored at 4 °C.

The particle size and zeta potential of the PCM@AuNPs were determined via dynamic light scattering (DLS) analysis via a Malvern NANO ZS instrument. The UV−vis absorption spectra of each component of the PCM@AuNPs were measured via a UV spectrophotometer. To standardize AuNPs concentration in PCM@AuNPs complexes, serial dilutions of AuNPs (0–50 μg/mL in PBS) were prepared. UV-vis absorption spectra (400–800 nm) were recorded. The absorbance at the AuNPs plasmon resonance peak (λ = 520 nm) was plotted against known concentrations to generate a linear calibration curve ($R^2 > 0.99$). For PCM@AuNPs samples, free AuNPs were separated from bacteria via centrifugation (3,000 ×g, 10 min). The supernatant absorbance at 520 nm was measured and subtracted from the total AuNPs added to calculate the bound fraction. Binding efficiency (%) was defined as:

$$Binding\ Efficiency = \frac{[AuNPs]\,total - [AuNPs]\,free}{[AuNPs]\,total} * 100\%$$

PCM@AuNPs were stored in PBS at 4 °C, and their UV-vis absorption spectra were collected at 0 h and 72 h to analyze stability and potential aggregation behavior. Before transmission electron microscopy (TEM), the PCM@AuNPs samples were fixed with glutaraldehyde.

Evaluation of PCM viability post-treatment

The PCM strain was cultured to an OD_{600} of 0.4–0.6 at 37 °C. Bacterial suspensions were irradiated with varying doses of radiation (0 Gy, 2 Gy, 4 Gy, 6 Gy, 8 Gy, and 10 Gy). After irradiation, the bacteria were further incubated at 37 °C overnight (approximately 6–8 h). The cultures were collected, appropriately diluted, and plated for colony counting. Moreover,1 mL of PCM suspension (OD_{600} = 0.4–0.6) was transferred to a 24-well plate. Ultrasound irradiation was applied under varying parameters (see details in Thermal-Induced and Ultrasound-Induced CAT Expression) while maintaining the temperature at 45 °C. After 30 min of irradiation, the samples were incubated at 37 °C overnight. The OD_{600} of the mixture was measured to assess bacterial growth.

In vitro cytotoxicity assay of AuNPs on PCM

The PCM and the PCM@AuNPs were cocultured at 37 °C for 12 h, respectively. At different time points, the OD_{600} of the mixture was determined. Twelve hours later, a drop of the diluted sample was placed on a microscope slide. A microscope was used to locate the bacteria, and images of bacterial movement at different time points were recorded. The data analysis software NIS Elements D4.10.00 was used to calculate the movement rate, which was recorded as distance/time.

Tumor targeting of PCM@AuNPs

The concentration of PCM was adjusted to 1×10^7 CFU/ml. The DiR dye was added to the PCM solution (30 μl/mL) and incubated at 37 °C for 45 min. The bacterial mixture was washed with PBS until the supernatant was clear. The bacteria were injected into the tumor-bearing mice via the tail vein (1×10^7 CFU per mouse) ($n = 4$). At the given time points, the mice were imaged with an IVIS system (PerkinElmer, USA) to evaluate the biodistribution and tumor accumulation of bacteria. Forty-eight hours after intravenous injection, the tumor-bearing mice were sacrificed, and organs, including the heart, lung, liver, kidney, and spleen, and tumors were obtained for fluorescence signal detection via the same imaging system. Additionally, the accumulation of PCM in different organs was detected via clone counting. At 48 h after the administration of PCM@AuNPs, tumors, and organs were obtained, and the diluted grinds of each organ were cultured on LB-Agar plates for clone counting.

Evaluation of the effect of PCM@AuNPs on oxygen production

Three experimental groups were used: MG1655@AuNPs + US (M1), PCM (M2), and PCM@AuNPs + US (M3). Following ultrasound induction (1.6 W/cm², 1 MHz, 3 s ON, and 7 s OFF) for 30 min, the samples were incubated at room temperature for 6 h. The active proteins from engineered bacteria were extracted via a bacterial protein extraction kit (Sangon Biotech, China). The precise quantification and activity of CAT expressed

by the PCM@AuNPs were assessed via a Catalase Elisa Kit (ZCIBIO Technology Co., Ltd., China) and a Catalase Activity Kit (Nanjing Jiancheng Bioengineering Institute, China). After quantification, different high concentrations of CAT and H_2O_2 were mixed in 5 mL of hydrogen trichloride buffer (0.1 M, pH = 7.52) for the reaction. A balloon was attached to one end of the test tube, and the volume of oxygen was determined by measuring the diameter of the oxygen-carrying ball. A dissolved oxygen monitor was used to reflect the real-time change in oxygen solubility directly. Which was purchased from Shanghai INESA Scientific Instruments Co., Ltd. (China)

To verify the ability of PCM@AuNPs to relieve hypoxia in tumors, the 4T1 tumor-bearing mice were divided into three groups: control, PCM@AuNPs, and PCM@AuNPs + US. The mice were i.v. Injected with 100 μL of PBS or PCM@AuNPs, and the number of bacteria was 1×10^7 CFU/100 μL. At 24 h p.i., each mouse in the PCM@AuNPs + US group was subjected to ultrasound (1.6 W/cm^2, 1 MHz, 3 s ON, and 7 s OFF irradiation) for 30 min. Six hours later, the tumor tissue was collected, and western blotting was used to confirm CAT expression in vivo. The tumor tissue was collected and sacrificed for immunofluorescence staining, with DAPI for the cell nucleus and HIF-1α for hypoxia-inducible factors. Images were obtained via CLSM.

In vitro detection of reactive oxygen species and DNA damage

To detect the generation of ROS and DNA damage induced by PCM@AuNPs during radiation in vitro. 4T1 cells were seeded into 24-well plates overnight at a density of 1×10^4 per well. After that, the cells were divided into seven groups: the control group without any treatment (G1) and the other groups were irradiated by X-ray at 6 Gy after being treated with PBS (G2), PCM (G3), AuNPs (G4), MG1655@AuNPs + US (G5), PCM@AuNPs (G6), or PCM@AuNPs + US (G7) at 37 °C with 5% CO_2 for 4 h. Subsequently, DCFH-DA, γ-H2AX, and the DNA ladder assay were used for ROS or DNA damage detection, respectively. Fluorescence imaging was conducted using a fluorescence microscope (EVOS M5000, America), and fluorescence intensity was quantified with ImageJ. Gel imaging was conducted under UV light using a ChemiDoc MP Imaging System (Bio-Rad, USA).

In vitro detection of the MMP

To assess the intracellular MMP. 4T1 cells were cocultured with the same treatment described above in 24-well plates. Then, 1 mL of JC-1 was added to the cells for coculture at 1 h after irradiation, and the cells were observed under a fluorescence microscope.

In vitro colony formation assay

4T1 cells (1,000/well) were seeded in 6-well plates and incubated with the different treatments mentioned above for 6 h. The samples were subsequently irradiated with γ-rays at a dose of 6 Gy. Next, the cells were continuously cultured with fresh drug-free medium in an incubator for another 5–8 days. The fixed colonies were then stained with crystal violet (0.25% ethanol) to subsequently count the number of colonies and evaluate the colony inhibition ability of each treatment.

Assessment of cell apoptosis

Cell apoptosis was determined with an Annexin V-FITC apoptosis detection kit. First, 4T1 cells at a density of 2×10^5 were seeded in 6-well plates. After the treatment described above, the cells were trypsinized and resuspended in 500 μL of binding buffer. Five microliters of Annexin V-FITC (20 μg/mL) and 5 μL of PI (50 μg/mL) were continuously added to the above buffers and then incubated for 15 min at room temperature in the dark. Finally, the degree of cell apoptosis in each group was analyzed via flow cytometry.

Cell cytotoxicity assay

4T1 cells were plated onto 96-well plates at a density of 1×10^4 cells per well at 37 °C in a 5% CO_2 incubator. Following the previous grouping. After the addition of 10 μL of Cell Counting Kit-8 to each well, the mixture was incubated for 2 h in a cell incubator. Cell proliferation was measured by measuring the optical density (OD) at 450 nm via a microplate reader.

In vivo antitumor assay

The 4T1 tumor-bearing mice with an approximate tumor volume of 100 mm^3 were randomly divided into five groups ($n = 4$): the control group (T1), RT group (T2), AuNPs + RT (T3), PCM + RT + US (T4), and PCM@AuNPs + RT + US (T5) groups. A total of 1×10^7 PCM in 100 μl of PBS was injected intravenously into tumor-bearing mice in the T4 and T5 groups. The T1 group was injected with 100 μl of PBS, and the concentration of AuNPs was 50 μg/ml. After 24 h of bacterial injection, the mice were irradiated with ultrasound (1.6 W/cm^2, 1 MHz, 3 s ON, and 7 s OFF irradiation times) to induce PCM for 30 min. Each group received a dose of 6 Gy of γ-ray irradiation on the third day, with a treatment cycle of 4 days, and the tumor volume and mouse weight were recorded every 2 days. The formula for calculating tumor volume was as follows: volume = (tumor length × tumor width^2)/2. After the mice died, the tumors were collected for H&E staining and TUNEL assays.

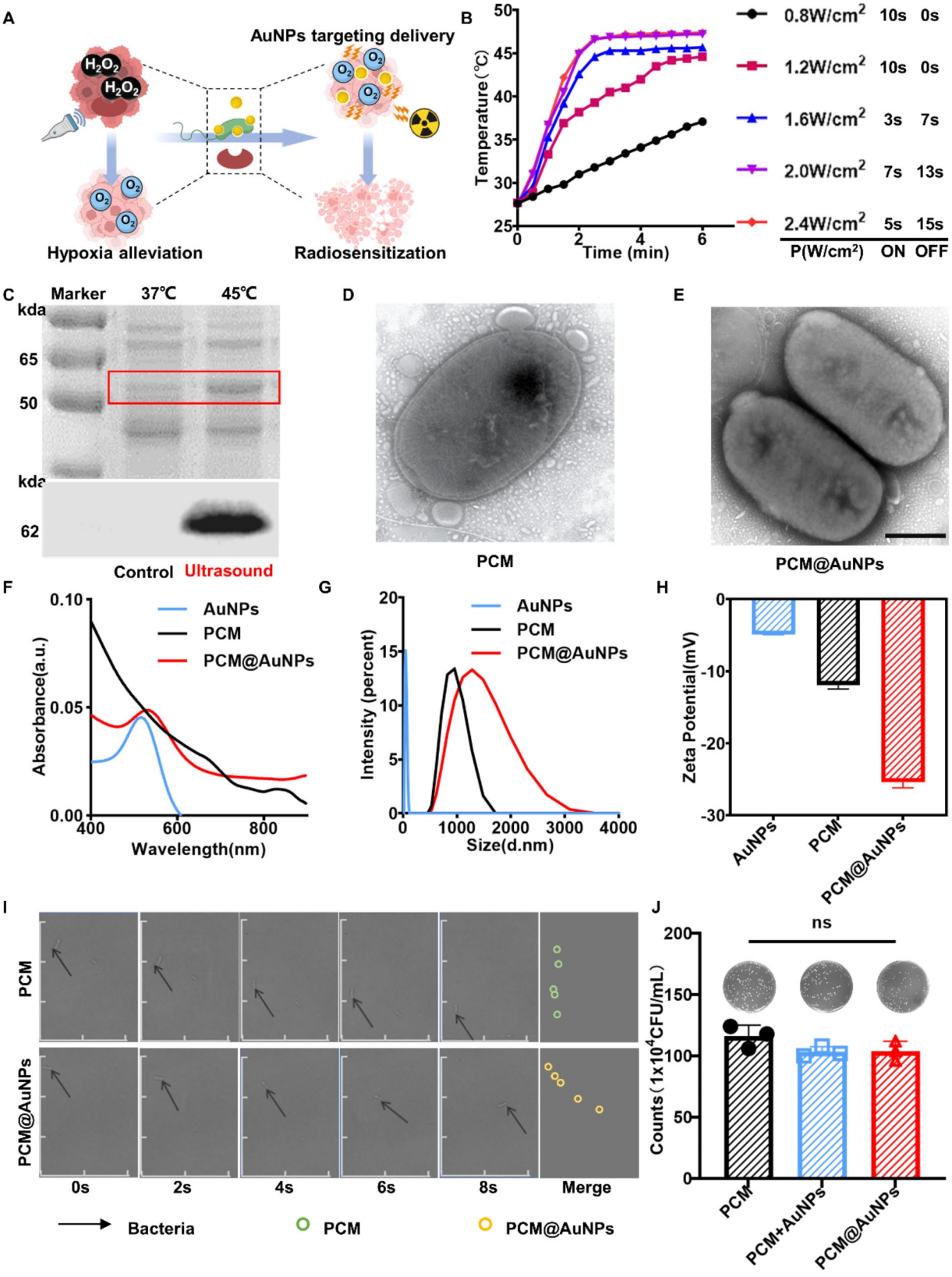

Fig. 2 (See legend on next page.)

(See figure on previous page.)

Fig. 2 Characterization of PCM@AuNPs. **A:** PCM@AuNPs are engineered to alleviate tumor hypoxia and enhance the delivery of AuNPs, thereby achieving efficient radiosensitization. **B:** Exploration of ultrasonic heating parameters. **C:** Expression of the CAT protein by ultrasound. **D-E**: TEM images of PCM (**D**) and PCM@AuNPs (**E**). **F**: Ultraviolet spectrophotometer of PCM@AuNPs. **G-H**: Size (**G**) and zeta potential (**H**) of AuNPs, PCM, and PCM@AuNPs. **I**: Migration capacity measurement of PCM@AuNPs and PCM. **J**: The number of bacterial monoclonal colonies generated by PCM, PCM + AuNPs, and PCM@AuNPs. Statistical analysis was performed via one-way ANOVA and Tukey's test (****$P < 0.0001$; ** $P < 0.01$; * $P < 0.05$)

Metastasis treatment

For lung metastasis treatment, the treated mice ($n = 4$) were euthanized on the 21st day by carbon dioxide asphyxiation, and their lungs were collected. The number of metastatic nodules in the lungs and the lung weight were recorded. The lung slices were then stained with H&E to observe the metastatic foci.

Statistical analysis

The statistical analyses of the experimental data were conducted via GraphPad Prism software version 9.5.0. The data set was subjected to one-way analysis of variance (ANOVA) for statistical evaluation, and the *P* values were determined via a two-tailed unpaired heteroscedastic t-test, with significance indicated by $^{*}P < 0.05$, $^{**}P < 0.01$, $^{***}P < 0.001$, and $^{****}P < 0.0001$.

Results

Preparation and characterization of PCM@AuNPs

The PCM@AuNPs, composed of PCM and AuNPs, were designed to alleviate tumor hypoxia and enhance the delivery of AuNPs, thereby achieving efficient radiosensitization (Fig. 2A). To facilitate noninvasive remote control of PCM CAT expression via focused ultrasound, the PBV220-CAT plasmid was transferred into *E. coli* MG1655 to induce high expression of CAT. A series of acoustic parameters, including sound intensity and the duration of irradiation in the ON/OFF states, were optimized. The results indicated that a sound intensity of 1.6 W/cm² with an ON time of 7 s and an OFF time of 13 s maintained the bacterial mixture at a constant temperature of 45 °C (Fig. 2B). SDS–PAGE analysis revealed significant expression of the CAT protein (62 kDa) in the PCM after a 45-minute treatment at 45 °C. In contrast, minimal CAT protein expression was observed at body temperature (37 °C). Upon ultrasound-induced PCM treatment at 1.6 W/cm² with the specified ON/OFF cycle, Western blotting revealed substantial CAT protein expression in the induced group, whereas minimal expression was detected in the uninduced group (Fig. 2C). Western blot analysis demonstrated sustained CAT protein expression for up to 24 h after induction (Figure S1).

To verify the successful construction of the PCM@AuNPs, transmission electron microscopy (TEM) was used to observe the interaction between the AuNPs and the PCM. The AuNPs were closely attached to the surface of the PCM, as shown in Fig. 2D-E. UV absorption measurements revealed that the AuNPs and PCM@AuNPs presented an absorption peak at 520 nm, confirming the successful construction of the PCM@AuNPs (Fig. 2F). Further morphological characterization revealed that the diameter of the PCM@AuNPs was approximately 1135.65 nm, with a zeta potential of -24.6 mV. In contrast, the average diameter of the AuNPs alone was 26.65 nm, with a zeta potential of -4.8 mV (Fig. 2G-H). The PCM@AuNPs stored in PBS at 4 °C for 72 h maintained their characteristic absorption peak ($\lambda = 520$ nm), confirming minimal aggregation. A minor intensity decrease (0.45 μg/mL AuNPs loss) indicated 94% retention on PCM carriers, demonstrating robust short-term stability (Figure S2).

To validate the tumor-targeting ability of the PCM@AuNPs, their motility was assessed to ensure efficient nanoparticle delivery to tumor sites. The migration abilities of the PCMs and PCM@AuNPs were compared over the same duration. The results revealed that the migration rate of the PCM was 18.3 μm/s, whereas the PCM@AuNPs exhibited a migration rate of 15.8 μm/s within 10 s (Fig. 2I). No significant differences in colony counts (Fig. 2J) or OD values (Figure S3) were observed at various time points between the PCM@AuNPs group and the PCM group, suggesting that the incorporation of nanoparticles did not adversely affect bacterial viability.

Experimental investigations into the effects of therapeutic parameters on PCM activity revealed that, although the liquid temperature was consistently maintained at 45 °C via controlled ultrasound on/off cycles, PCM treated with 2.4 W/cm² or 2.0 W/cm² ultrasound intensities exhibited significantly lower OD values compared to other treatment groups. In contrast, no statistically significant alterations in PCM activity were detected within the 1.6 W/cm² intensity range (Figure S4). Finally, after coculture, the cell viability remained above 80%, even at the highest concentration of 50 μg/ml, demonstrating that PCM@AuNPs exhibit low cytotoxicity toward 4T1 cells (Figure S5).

Improvements in cellular hypoxia and radiation deposition of PCM@AuNPs

To validate the hypoxia-alleviating function of PCM@AuNPs under ultrasound, quantitative ELISA revealed a 2.7-fold increase in CAT expression in the M3(PCM@AuNPs) group compared to the M2(PCM) group and a 2.4-fold increase compared to the M1(MG1655@AuNPs + US) group (Fig. 3A).

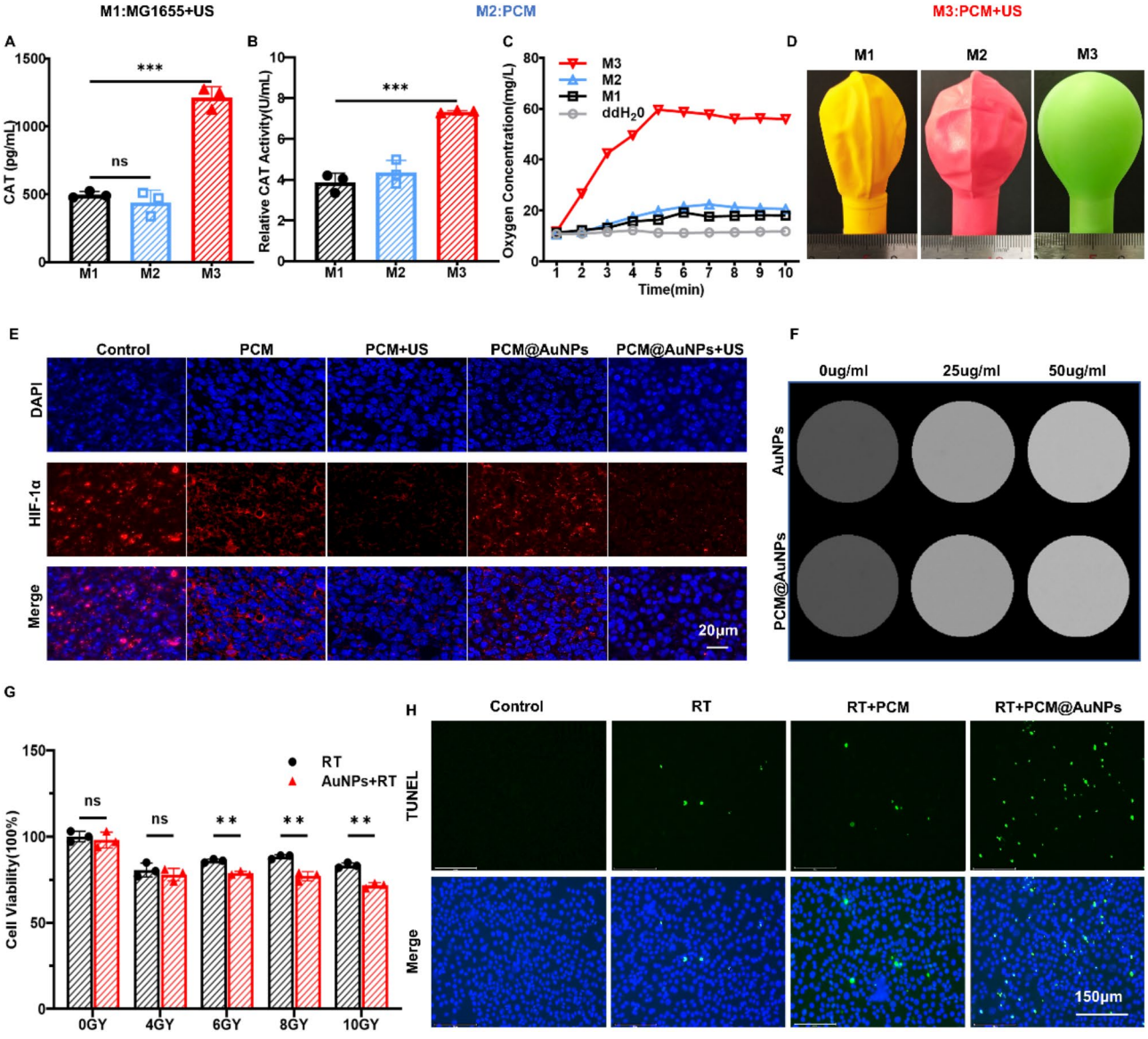

Fig. 3 Functional verification of PCM@AuNPs. **A:** The concentration of released CAT was determined via ELISA. **B:** Viability of CAT to decompose H_2O_2 in the MG1655@AuNPs + US (M1), PCM (M2), and PCM@AuNPs + US (M3). **C:** Oxygen production with time after adding different samples into the H_2O_2 solution. **D:** Oxygen production volume after adding different samples to the H_2O_2 solution. **E:** Assessment of the impact of ultrasound-induced PCM@AuNPs on HIF-1α expression within tumor tissue (scale bar: 20 μm). **F:** Evaluation of the CT imaging capability of PCM@AuNPs. **G:** Verification of the radiosensitizing effect of AuNPs under various radiation doses. **H:** TUNEL-DAPI co-staining for fluorescence detection (scale bar: 150 μm). Statistical analysis was performed via one-way ANOVA and Tukey's test (****$P < 0.0001$; ** $P < 0.01$; * $P < 0.05$)

The H_2O_2 decomposition capabilities of CAT expressed in the three groups were subsequently assessed to measure CAT activity. The results revealed that the M3 group presented the highest CAT activity, with an H_2O_2 decomposition capacity nearly double that of the other two groups (Fig. 3B). To further evaluate the oxygen production capacity of the PCM@AuNPs, a dissolved oxygen monitoring device was employed. The oxygen concentrations in both the M1 and M2 groups only slightly increased because of self-oxidation. In contrast, the M3 group achieved a significantly higher dissolved oxygen concentration of 59.86 mg/L at the 5-minute mark, which remained stable throughout the measurement period (Fig. 3C). Moreover, the M3 group produced the highest amount of O_2 in the H_2O_2 solution, resulting in the largest balloon volume, measured at 34.6705 cm^3, which was three times greater than that of the other groups (Fig. 3D). MG1655 actively targets tumor tissues. The in vivo fluorescence imaging results indicated that PCM@AuNPs are metabolized by the liver while specifically targeting tumors. After 24 h, the fluorescence signal in the liver began to decrease, whereas the tumor site continued

to exhibit increased fluorescence, suggesting effective accumulation at the tumor site. Subsequent tissue extraction and coating detection revealed a significantly greater bacterial count in tumor tissues than in other tissues (Figure S6-S7). The results of the Western blot analysis indicated that, when the cells were injected with PCM@AuNPs and induced by ultrasound, there was significant expression of CAT in the tumor tissue (Figure S8). Additionally, the expression of HIF-1α—a hypoxia-inducible transcription factor that stabilizes under low oxygen conditions to promote tumor angiogenesis and metabolic adaptation—was lower in the PCM + US and PCM@AuNPs groups than in the other groups (Fig. 3E).

CT imaging revealed concentration-dependent radiation attenuation by PCM@AuNPs. While both AuNPs and PCM@AuNPs at 0 mg/mL showed CT values comparable to soft tissue, their CT values significantly increased at 50 mg/mL (Fig. 3F). Under 6 Gy irradiation in normoxia, AuNPs reduced 4T1 cell survival from 86% (radiation alone) to 78% (Fig. 3G). No significant viability reduction was observed in RT or AuNPs groups at doses exceeding 6 Gy, thus, 6 Gy was selected for subsequent studies. The PCM@AuNPs + RT group exhibited transiently lower survival than RT alone at 0 and 12 h, though no difference persisted by 24 h (Figure S9). TUNEL-DAPI co-staining confirmed maximal apoptosis in the PCM@AuNPs-treated group (Fig. 3H). Furthermore, bacterial plating assays demonstrated a marked reduction in colony-forming units following irradiation doses of 8 Gy and 10 Gy (Figure S10).

Radiosensitization detection of PCM@AuNPs

Under hypoxic conditions, all groups underwent RT. The G7 group exhibited significantly higher ROS levels—evidenced by intensified green fluorescence—compared to G5 and G6 (Fig. 4A-B). Elevated ROS, synergizing with ionizing radiation, induces DNA damage proportional to intracellular ROS concentrations. DNA ladder electrophoresis confirmed the most severe DNA damage in G7, marked by distinct ladder bands absent in other groups (Fig. 4C). Consistently, double-strand break (DSB) detection revealed the strongest green fluorescence in G7, reflecting a high DSB burden and extensive DNA damage (Fig. 4D). ROS accumulation further triggered peroxidative mitochondrial membrane damage, reducing mitochondrial membrane potential (MMP) and causing dysfunction. G7 showed the highest green fluorescence (low MMP) and minimal red fluorescence, while G1 - G5 displayed strong red fluorescence (intact MMP) and negligible green signals (Fig. 4E-F).

In vitro antitumor effects of PCM@AuNPs

First, the radiosensitizing effect under hypoxic conditions was assessed through apoptosis detection. The results revealed that the G7 group had a high proportion of apoptotic cells (47.74%), whereas the G6 group, which was not subjected to ultrasound induction, exhibited only 18.63% apoptotic cells. The G1 group had the lowest proportion of apoptotic cells, at only 6.81% (Fig. 5A-B).

To verify whether this apoptotic phenomenon leads to cell death, further analysis was performed via the CCK-8 assay. Compared with the G6 group, the G7 group presented the lowest cell viability, with no significant difference, but a significant reduction in cell viability compared with the G1 group. This trend in cell viability was consistent with the results of the apoptosis assay (Fig. 5C).

To evaluate the long-term inhibitory effects of RT on cell growth, colony formation assays were performed following prolonged culture. The results indicated that the G7 group formed the fewest cell colonies, which was significantly different from the results of the other groups. The G1 group presented the lowest colony count, while no significant difference was observed between the G5 and G6 groups (Fig. 5D-E).

In vivo antitumor effects of PCM@AuNPs

The histopathological analysis of major organs (heart, liver, spleen, lung, and kidney) was showing that no significant pathological abnormalities, such as necrosis, inflammatory infiltration, or fibrosis in the PCM@AuNPs treated groups post-14d injection (Figure S11). During the 14-day RT treatment protocol, tumor dimensions and mouse body weights were monitored every two days (Fig. 6A). To verify the therapeutic efficacy of the treatments, a comparison with the control group was conducted. All the treatment groups exhibited suppressed tumor growth. In the T1 group, the tumors exhibited rapid growth posttreatment, with a ninefold increase in size by day 14. Notably, the T2 group, which received only 6 Gy of RT, showed no substantial suppression of tumor growth. In contrast, the T3 and T4 groups experienced only a 2.5-fold increase in tumor size, whereas the T5 group exhibited negligible tumor growth (Fig. 6B-C).

To further assess treatment efficacy, tumor weights were measured (Fig. 6D). The results revealed that tumors in the T5 group had the lowest weight, whereas those in the T1 group were the heaviest, which was consistent with the body weight measurements. Histological analysis, including H&E and TUNEL staining of tumor tissues, revealed extensive nuclear rupture, widespread cancer cell death, and pronounced inflammatory responses in the T5 group (Fig. 6E-F). Moreover, enumeration of pulmonary nodules revealed a significant reduction in the number of nodules in the T5 group compared with that in the groups treated with AuNPs, PCM, or RT alone (Fig. 6G-H). Importantly, no significant weight loss was observed throughout the treatment period, and the

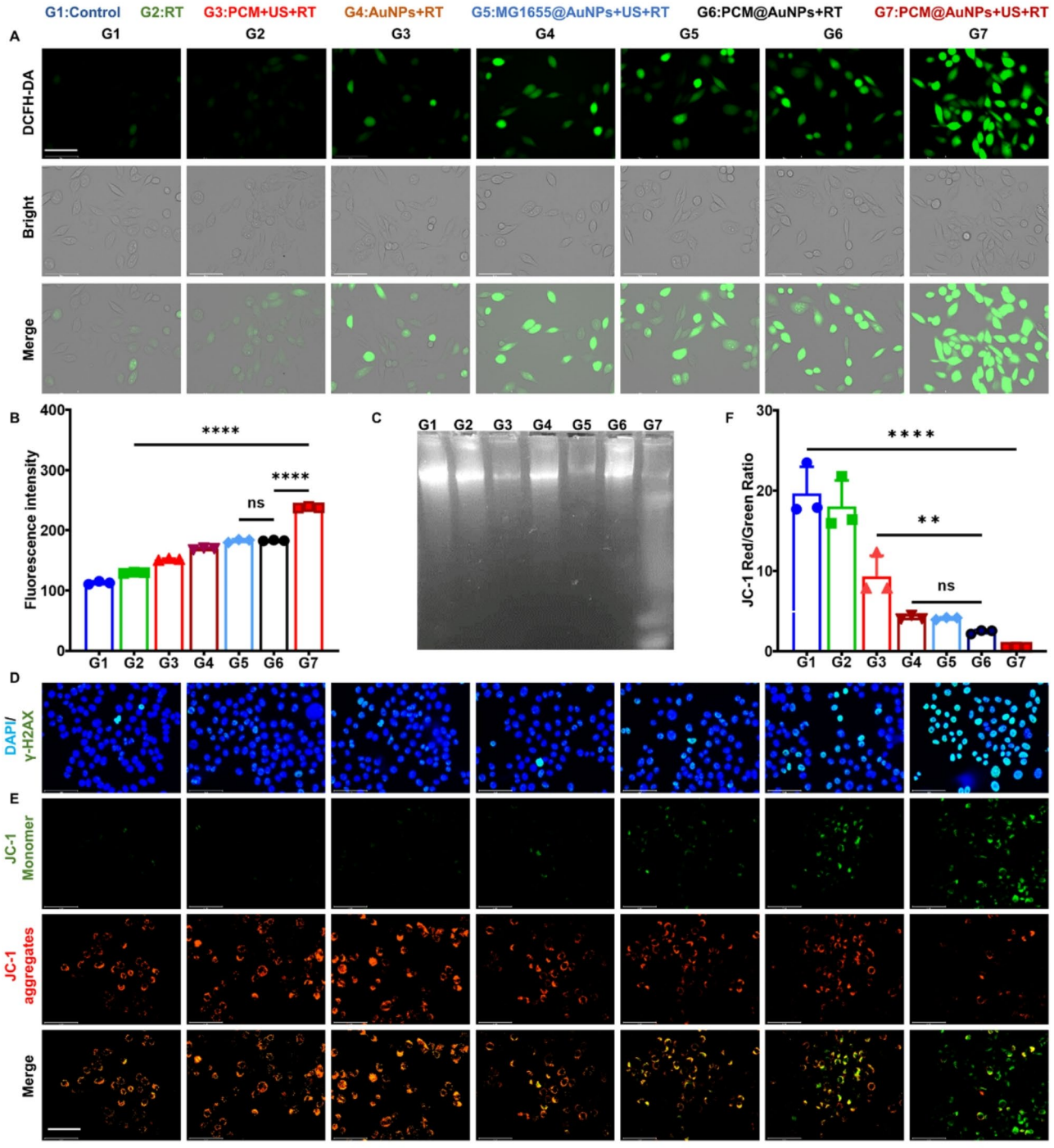

Fig. 4 Radiosensitization of PCM@AuNPs. **A-B**: ROS production of 4T1 cells in different treatment groups detected with a DCFH-DA fluorescent probe (scale bar: 75 μm). **C:** DNA ladder electrophoresis was used to detect cell apoptosis. **D:** Images of γ-H2AX immunofluorescence-labeled 4T1 cells after exposure to irradiation. The samples were stained with DAPI (blue) and γ-H2AX (green) (scale bar: 75 μm). **E-F**: Fluorescence microscopy images of the MMP after different treatments in JC-1-stained cells (**E**) and JC-1 Red/Green ratio analysis (**F**), JC-1 Red/Green ratio analysis was performed via ImageJ software. (scale bar: 75 μm). Statistical analysis was performed via one-way ANOVA and Tukey's test (****$P < 0.0001$; ** $P < 0.01$; * $P < 0.05$)

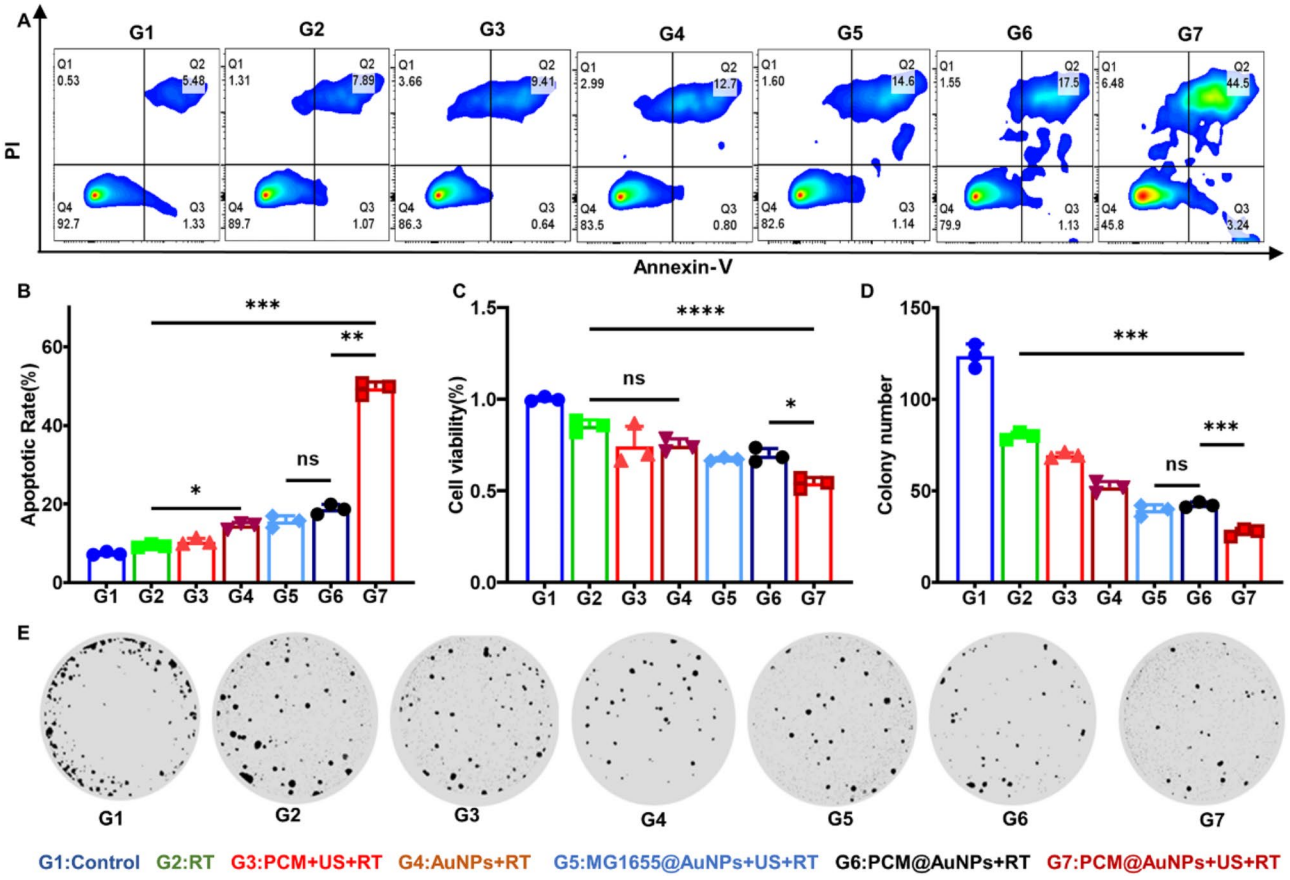

Fig. 5 In vitro antitumor effects of PCM@AuNPs. **A-B**: Flow cytometry was used to measure cell apoptosis in response to different treatments (**A**). The data were analyzed via FlowJo (**B**). **C:** Viability of 4T1 cells in different treatment groups. **D-E**: Colonies of 4T1 cells treated via different methods (**E**). The data were analyzed via ImageJ (**D**). Statistical analysis was performed via one-way ANOVA and Tukey's test (****$P < 0.0001$; ** $P < 0.01$; * $P < 0.05$)

weight differences between the groups were statistically insignificant (Figure S12).

Discussion

In this study, we developed an integrated nanosystem (PCM@AuNPs) to achieve more effective RT sensitization through multiple pathways. The integrated nanosystem composed of engineered bacteria and gold nanoparticles could effectively improve the delivery efficiency and specific accumulation of radiosensitizers and relieve hypoxic conditions in the TME, enhancing cancer cell apoptosis induced by RT and significantly inhibiting tumor growth.

The hypoxic, nutrient-rich and immunosuppressive TME supplies an appropriate growth environment for PCM. Firstly, PCM tend to migrate towards the hypoxic zone of tumors, the active mechanisms likely involve some chemotactic factors (e.g. clusterin, serglycin, and TGF-β2) generated by dying tumor cells in the low oxygen lesions. Secondly, the nutritious TME is uniquely attractive to bacteria. PCM can sense high density of nutrients in and around the tumor core through chemoreceptors, and accumulate at both sites. Moreover, the immunosuppressive environment facilitates the bacteria dissemination in tumors, and depleting host neutrophils further increases bacteria accumulation and spread throughout the tumors [30]. Bacteria specifically target and colonize tumor sites, making them promising carriers for AuNPs aimed at enhancing radiation energy deposition and amplifying the effects of RT within tumors. Our findings demonstrate that AuNPs are chemically conjugated onto the surface of bacterial carriers—PCM—for targeted delivery in the context of RT. The PCM@AuNPs system effectively retains the viability of the PCM micromotors. This aligns with previous work by Du et al., who developed a bacteria-driven drug delivery system utilizing *E. coli* as a biological carrier for targeted delivery of DOX-PFP-PLGA [31]. However, the long-term biocompatibility of engineered bacteria remains a critical concern, as sustained colonization in hypoxic tumor regions may lead to chronic toxicity through unintended metabolite accumulation. Additionally, repeated administration risks triggering innate immune hyperactivation via pathogen-associated molecular patterns (PAMPs)

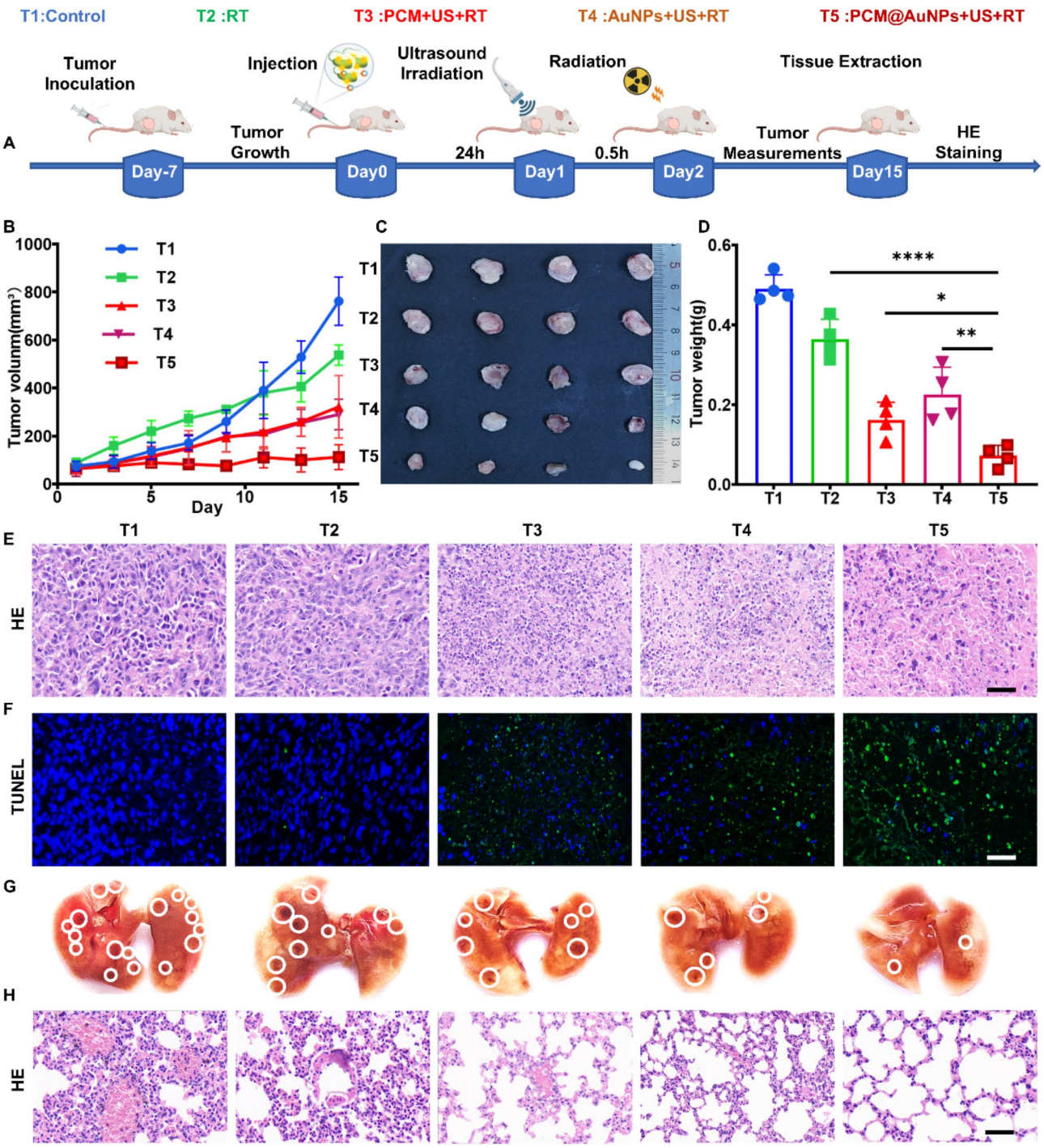

Fig. 6 In vivo antitumor effects of PCM@AuNPs. **A:** Schematic diagram of the antitumor experiment in vivo. **B:** Tumor growth profiles of the mice subjected to different treatments. **C**: Representative photographs of tumors after various treatments. **D:** Weights of mouse tumors after various treatments. **E-F**: H&E staining (**E**) and TUNEL staining (**F**) images of tumor slices obtained from different mice treated under various conditions (scale bar = 100 μm). **G-H**: Images of lung nodules (**G**) and H&E-stained images (**H**) of lung tissues from mice subjected to different methods (scale bar = 100 μm). Statistical analysis was performed via one-way ANOVA and Tukey's test (****$P < 0.0001$; ** $P < 0.01$; * $P < 0.05$)

and adaptive immune responses, resulting in neutralizing antibody production and accelerated bacterial clearance. To address these challenges, Wang et al. used low immunogenicity and long circulation of erythrocyte membrane coated with engineered bacteria to improve the long-term biocompatibility and therapeutic efficacy of engineered bacteria [32].

As effective radiosensitizers, AuNPs significantly increase cancer cell apoptosis induced by RT. When the effects of AuNPs were compared with those of the gold nanoclusters (c(RGDyC)-AuNCs) constructed by Liang et al., it was observed that the AuNPs had a similar RT efficiency at a dose of 4 Gy, although they were less effective at 6 Gy and 8 Gy [33]. The hydrodynamic diameter (HD) of the AuNCs was determined to be 3.2 ± 0.54 nm, whereas the diameter of the AuNPs was approximately eight times larger, which may account for this difference in efficiency. Recent theoretical studies have shown that the relative level of radiosensitization of AuNPs decreases significantly as the nanoparticle size increases [34]. The potential mechanism underlying this phenomenon may involve size-dependent variations in the relative electron density of AuNPs, which arise from nanoscale surface-to-volume ratio effects. Specifically, reduced particle dimensions enhance surface atom contributions, increasing electron density gradients at the nanoparticle interface. This localized electron density modulation could amplify X-ray attenuation efficiency through enhanced photoelectric absorption cross-sections, thereby governing radiation dose enhancement effects in AuNP-mediated radiosensitization [35]. Therefore, the selection of gold nanoparticles with better size is the improvement direction of subsequent research. It is worth mentioning that our AuNPs were obtained commercially, the radiosensitization properties of standardized AuNPs met the requirements of previous literature, but pre-coated PEG limited the efficiency of further functionalization. At the same time, commercially available AuNPs only offer standard spherical and fixed particle sizes, it is difficult to evaluate the morphologic dependent radiosensitization mechanisms such as tip enhancement. Ultrasound has been widely used for rapid, scalable, and controlled nanoparticle synthesis. The properties of AuNPs synthesized via ultrasound-assisted methods are critically influenced by three key parameters. Frequency directly affects the size and uniformity of AuNPs. Power intensity governs both the size distribution of the nanoparticles and the efficiency of ligand adsorption onto their surfaces. Meanwhile, the type of cavitation influences the stability and functionalization outcomes of the AuNPs. Studies demonstrate sonochemical synthesis enables precise control over AuNP properties by strategically optimizing these parameters. It will provide more options for improving the radiosensitization properties of AuNPs [36–38]. Moreover, the PCM@AuNPs preserve the therapeutic properties of the AuNPs, which shows a similar deposition of radiation energy at various AuNP concentrations. These results are consistent with research by Pan et al., who designed a smart bacteria-based nanosystem with engineered bacteria combined with high-atomic-number (high-Z) materials on the surface [20].

Despite advances, developing a radiotherapy sensitization system that inhibits DNA repair mechanisms through multiple pathways remains critical. Hypoxia, a hallmark of solid tumors, can be reversed by CAT-mediated decomposition of H_2O_2 [39]. Engineered bacteria expressing CAT have been explored. Ding et al. investigated CAT-expressing *E. coli*, and the release of CAT occurred following the destruction of the bacterial membranes via laser irradiation, which may adversely impact bacterial colonization [40]. Choosing a minimally invasive protein expression method will enable engineered bacteria to continuously express the CAT protein within tumors [12]. The use of isopropyl-β-thiogalactoside (IPTG) facilitates sustainable CAT production [41]. However, since IPTG is often administered via intravenous injection, its nonspecific spatial accumulation and the uncertainty regarding the timing of tumor targeting can result in CAT expression in nontumor tissues, adversely affecting normal physiological functions [42, 43]. In contrast, ultrasound offers a noninvasive, spatially precise alternative. Here, ultrasound-controlled CAT expression in the PCM strain was achieved. The CAT gene was inserted under tandem promoters PL/PR, which are activated by high temperatures. Our results indicate that ultrasound exposure generated localized heat, elevating the bacterial microenvironment to 45 °C. Thermal activation of PL/PR promoters triggered CAT expression, enabling H_2O_2 decomposition. This approach aligns with Chen et al.'s ultrasound-activated IFN-γ expression system, confirming the versatility of acoustic control in bacterial gene regulation. Their study found that after ultrasound irradiation, the expression of mCherry fluorescent protein maintained up to 3 days, demonstrating the long-term stability of bacterial gene expression induced by this method [28].

Based on the hypoxia-alleviating effects of CAT, we systematically investigated its regulatory impact on HIF-1α pathway activation and oxidative stress dynamics. To delineate CAT-specific contributions, a dedicated PCM group was incorporated into the experimental design. Consistent with the findings of Meng et al., [44] Our findings revealed that ultrasound-induced CAT expression by PCM achieved two critical outcomes in tumor tissues: localized oxygen generation through H_2O_2 decomposition significantly reduced HIF-1α accumulation, attributable to restored prolyl hydroxylase activity and subsequent VHL-mediated proteasomal degradation,

while the liberated molecular oxygen paradoxically enhanced ROS generation via revived mitochondrial electron transport chain activity, amplifying oxidative stress pathways. This synergistic approach, which addresses both the metabolic adaptation of tumors and their resistance to apoptosis, overcoming hypoxia-related radiotherapy limitations.

Through multiple pathways of enhancing radiation deposition and alleviating tumor hypoxia, PCM@AuNPs demonstrated significant radiosensitizing effects both in vitro and in vivo. As a bio/nonbiohybrid system, it exhibited good biocompatibility. We found that PCM@AuNPs could enhance RT efficiency through the absorption of more radiation and the generation of more ROS, leading to an increase in DSBs and disruption of the mitochondrial membrane potential, thereby causing the release of cytochrome C and activating the apoptosis pathway. The mitochondrial damage can be detected by JC-1, In healthy mitochondria, JC-1 forms aggregates in the mitochondrial matrix, emitting strong red fluorescence. When mitochondrial membrane potential collapses due to ROS-induced damage, JC-1 remains in the cytoplasm as monomers, emitting green fluorescence [45]. Mechanistically, ultrasound-activated PCM@AuNPs triggered mitochondrial dysfunction (Fig. 4E), leading a suppression of both primary tumor progression and pulmonary metastatic dissemination.

Although PCM@AuNPs + US can achieve significant radiosensitization effects and good safety, several steps need to be determined for future clinical applications. The mechanisms of lung metastasis inhibition have not yet been explored. Moreover, combining this radiosensitization strategy with other treatment methods is necessary [46]. As we have observed, the increase in ROS production may lead to an increase in ICD occurrence, which, along with HIF-1α, can affect tumor metastasis [12, 47]. Therefore, combining immunotherapy and further exploring the underlying mechanisms will help us discover a more effective combination therapy strategy for treating tumors.

Conclusions

In summary, an effective strategy based on an integrated nanosystem (PCM@AuNPs) for radiosensitization through multiple pathways was developed, which employed the PCM to improve the delivery efficiency of radiosensitizers and express CAT in the acoustic control of ultrasound, effectively decomposing H_2O_2 and thereby increasing the oxygen concentration, thereby alleviating specific hypoxia. Our study revealed that the combination of PCM@AuNPs + RT significantly inhibited tumor growth and metastasis. In conclusion, we have established a highly effective strategy for radiosensitization by integrating PCM@AuNPs with focused ultrasound.

Abbreviations

RT	Radiotherapy
ROS	Reactive oxygen species
AuNPs	Gold nanoparticles
CAT	Catalase
TME	Tumor microenvironment
US	Ultrasound
DiR	1,1-dioctadecyl-3,3,3,3-tetramethylindotricarbocyanine iodide
EDC	1-Ethyl-3-(3-(dimethylamino)propyl) carbodiimide
sulfo-NHS	n-hydroxysuccinimide
DMEM	Dulbecco's modified Eagle's medium
FBS	Fetal bovine serum
MMP	Mitochondrial membrane potential
IPTG	Isopropyl-β-thiogalactoside

Supplementary Information

The online version contains supplementary material available at https://doi.org/10.1186/s12951-025-03329-7.

Supplementary Material 1

Acknowledgements

Not applicable.

Author contributions

LL: Writing – review & editing, Writing – original draft, Visualization, Validation, Methodology, Investigation, Formal analysis, Data curation, Conceptualization. HX: Writing – original draft, Writing – original draft, Visualization, Validation, Investigation, Formal analysis. MD: Writing—review & editing, conceptualization, supervision, resources, funding acquisition. ZC: Writing–review & editing, Supervision, Resources, Funding acquisition, Project administration. All the authors read and approved the final manuscript.

Funding

This work was supported by the National Natural Science Foundation of China (82272028, 82102087), National Key R&D Program of China (2019YFE0110400), and Hunan Provincial Health High-Level Talent Scientific Research Project (R2023010).

Data availability

Data is provided within the manuscript or supplementary information files.

Declarations

Ethics approval and consent to participate

All experimental protocols received approval from the Medical Ethics Committee at the University of South China. Animal-related procedures adhered to ethical guidelines established by the Experimental Animal Welfare Ethics Committee of the University of South China (USC2024XS267).

Consent for publication

Not applicable.

Competing interests

The authors declare no competing interests.

Received: 26 November 2024 / Accepted: 14 March 2025
Published online: 29 March 2025

References

1. Atun R, Jaffray DA, Barton MB, Bray F, Baumann M, Vikram B, et al. Expanding global access to RT. Lancet Oncol. 2015;16(10):1153–86.
2. Her S, Jaffray DA, Allen C. Gold nanoparticles for applications in cancer radiotherapy: mechanisms and recent advancements. Adv Drug Deliv Rev. 2017;109:84–101.

3. Yao Y, Xu R, Shao W, Tan J, Wang S, Chen S, et al. A novel nanozyme to enhance radiotherapy effects by lactic acid scavenging, ROS generation, and hypoxia mitigation. Adv Sci. 2024;11(26):e2403107.
4. Suwa T, Kobayashi M, Nam J-M, Harada H. Tumor microenvironment and radioresistance. Exp Mol Med. 2021;53(6):1029–35.
5. Telarovic I, Wenger RH, Pruschy M. Interfering with tumor hypoxia for radiotherapy optimization. J Experimental Clin Cancer Res. 2021;40(1):197.
6. Yin W, Qiang M, Ke W, Han Y, Mukerabigwi JF, Ge Z. Hypoxia-responsive block copolymer radiosensitizers as anticancer drug nanocarriers for enhanced chemoradiotherapy of bulky solid tumors. Biomaterials. 2018;181:360–71.
7. Wang H, Mu X, He H, Zhang X-D. Cancer radiosensitizers. Trends Pharmacol Sci. 2018;39(1):24–48.
8. Bhat V, Pellizzari S, Allan AL, et al. Radiotherapy and radiosensitization in breast cancer: molecular targets and clinical applications. Crit Reviews Oncology/ Hematol. 2022;169:103566.
9. Xu H, Liu Z, Du M, Chen Z. Progression in low-intensity ultrasound-induced tumor radiosensitization. Cancer Med. 2024;13(13):e7332.
10. Liu Y, Zhang P, Li F, et al. Metal-based nanoenhancers for future radiotherapy: radiosensitizing and synergistic effects on tumor cells. Theranostics. 2018;8(7):1824–49.
11. Zhang Y, Huang F, Ren C, et al. Enhanced radiosensitization by gold nanoparticles with Acid-Triggered aggregation in cancer radiotherapy. Adv Sci. 2019;6(8):1801806.
12. Du M, Wang T, Peng W, Feng R, Goh M, Chen Z. Bacteria-driven nanosonosensitizer delivery system for enhanced breast cancer treatment through sonodynamic therapy-induced Immunogenic cell death. J Nanobiotechnol. 2024;22(1):167.
13. Jiménez-Jiménez C, Moreno VM, Vallet-Regí M. Bacteria-Assisted transport of nanomaterials to improve drug delivery in cancer therapy. Nanomaterials. 2022;12(2):288.
14. Adewale OB, Davids H, Cairncross L, Roux S. Toxicological behavior of gold nanoparticles on various models: influence of physicochemical properties and other factors. Int J Toxicol. 2019;38(5):357–84.
15. Xie J, Gong L, Zhu S, Yong Y, Gu Z, Zhao Y. Emerging strategies of Nanomaterial-Mediated tumor radiosensitization. Adv Mater. 2019;31(3):e1802244.
16. Gholami A, Mohkam M, Soleimanian S, Sadraeian M, Lauto A. Bacterial nanotechnology as a paradigm in targeted cancer therapeutic delivery and immunotherapy. Microsystems Nanoengineering. 2024;10:113.
17. Chen F, Zang Z, Chen Z, Cui L, Chang Z, Ma A, et al. Nanophotosensitizer-engineered Salmonella bacteria with hypoxia targeting and photothermal-assisted mutual bioaccumulation for solid tumor therapy. Biomaterials. 2019;214:119226.
18. Chen W, Wang Y, Qin M, Zhang X, Zhang Z, Sun X, et al. Bacteria-Driven hypoxia targeting for combined biotherapy and photothermal therapy. ACS Nano. 2018;12(6):5995–6005.
19. Zhu Z, Liu Q, Zhu K, Wang K, Lin L, Chen Y, et al. Aggregation-induced emission photosensitizer/bacteria biohybrids enhance Cerenkov radiation-induced photodynamic therapy by activating anti-tumor immunity for synergistic tumor treatment. Acta Biomater. 2023;167:519–33.
20. Pan P, Dong X, Chen Y, Zeng X, Zhang X-Z. Engineered bacteria for enhanced radiotherapy against breast carcinoma. ACS Nano. 2022;16(1):801–12.
21. Li Y, Yun K-H, Lee H, Goh S-H, Suh Y-G, Choi Y. Porous platinum nanoparticles as a high-Z and oxygen generating nanozyme for enhanced radiotherapy in vivo. Biomaterials. 2019;197:12–9.
22. Chen Y, Zhong H, Wang J, Wan X, Li Y, Pan W, et al. Catalase-like metal–organic framework nanoparticles to enhance radiotherapy in hypoxic cancer and prevent cancer recurrence. Chem Sci. 2019;10(22):5773–8.
23. Najafi A, Keykhaee M, Khorramdelazad H, Karimi MY, Nejatbakhsh Samimi L, Aghamohamadi N, et al. Catalase application in cancer therapy: simultaneous focusing on hypoxia Attenuation and macrophage reprogramming. Biomed pharmacotherapy = Biomedecine Pharmacotherapie. 2022;153:113483.
24. Yang N, Xiao W, Song X, Wang W, Dong X. Recent advances in tumor microenvironment hydrogen Peroxide-Responsive materials for cancer photodynamic therapy. Nano-micro Lett. 2020;12(1):15.
25. Liu Q, Zhang A, Wang R, Zhang Q, Cui D. A review on metal- and metal Oxide-Based nanozymes: properties, mechanisms, and applications. Nano-Micro Lett. 2021;13(1):154.
26. Wu G, Yan Q, Jones JA, Tang YJ, Fong SS, Koffas MAG. Metabolic burden: cornerstones in synthetic biology and metabolic engineering applications. Trends Biotechnol. 2016;34(8):652–64.
27. Yang Y, Wang Y, Zeng F, Chen Y, Chen Z, Yan F. Ultrasound-visible engineered bacteria for tumor chemo-immunotherapy. Cell Rep Med. 2024;5(5):101512.
28. Chen Y, Du M, Yuan Z, Chen Z, Yan F. Spatiotemporal control of engineered bacteria to express interferon-γ by focused ultrasound for tumor immunotherapy. Nat Commun. 2022;13(1):4468.
29. Liu Z, Lei L, Zhang Z, Du M, Chen Z. Ultrasound-responsive engineered bacteria mediated specific controlled expression of catalase and efficient radiotherapy. Mater Today Bio. 2025;31:101620.
30. Lin D, Feng X, Mai B, Li X, Wang F, Liu J, Liu X, Zhang K, Wang X. Bacterial-based cancer therapy: an emerging toolbox for targeted drug/gene delivery. Biomaterials. 2021;277:121124.
31. Du M, Wang T, Feng R, Zeng P, Chen Z. Establishment of ultrasound-responsive sonobacteriabot for targeted drug delivery and controlled release. Front Bioeng Biotechnol. 2023;11:1144963.
32. Qiao C, Wang L, Huang C, Wang Z. Engineered bacteria manipulate cysteine metabolism to boost Ferroptosis-Based pancreatic ductal adenocarcinoma therapy. Adv Mater. 2025;37(6):e2412982.
33. Liang G, Jin X, Zhang S, Xing D. RGD peptide-modified fluorescent gold nanoclusters as highly efficient tumor-targeted radiotherapy sensitizers. Biomaterials. 2017;144:95–104.
34. Hossain M, Su M. Nanoparticle location and Material-Dependent dose enhancement in X-ray radiation therapy. J Phys Chem C. 2012;116(43):23047–52.
35. Dou Y, Guo Y, Li X, Li X, Wang S, Wang L, Lv G, Zhang X, Wang H, Gong X, Chang J. Size-Tuning ionization to optimize gold nanoparticles for simultaneous enhanced CT imaging and radiotherapy. ACS Nano. 2016;10(2):2536–48.
36. Mohammed AD, Azlan AA, Mahmood SJ, Khaniabadi PM, Mehrdel B. Sonochemical-assisted synthesis of highly stable gold nanoparticles catalyst for decoloration of methylene blue dye. Inorg Chem Commun. 2021;127:1387–7003.
37. Dheyab MA, Aziz AA, Khaniabadi PM, Jameel MS. Potential of a sonochemical approach to generate MRI-PPT theranostic agents for breast cancer. Photodiagn Photodyn Ther. 2021;33:102177.
38. Mohammed AD, Azlan AA, Mahmood SJ. Synthesis and optimization of the sonochemical method for functionalizing gold shell on Fe3O4 core nanoparticles using response surface methodology. Surf Interfaces. 2020;21:2468–0230.
39. Xu H, Guo Z, Li M, Du M. Mirna Marques bezerra. Copper-Based nanomaterials for Image-Guided cancer therapy. BIO Integr. 2024;5(1).
40. Ding S, Liu Z, Huang C, Zeng N, Jiang W, Li Q. Novel engineered bacterium/black phosphorus quantum Dot hybrid system for hypoxic tumor targeting and efficient photodynamic therapy. ACS Appl Mater Interfaces. 2021;13(8):10564–73.
41. Wang T, Du M, Yuan Z, Guo J, Chen Z. Multi-functional nanosonosensitizer-engineered bacteria to overcome tumor hypoxia for enhanced sonodynamic therapy. Acta Biomater. 2024;189:519–31.
42. Gebicka L, Krych-Madej J. The role of catalases in the prevention/promotion of oxidative stress. J Inorg Biochem. 2019;197:110699.
43. Zamocky M, Furtmüller PG, Obinger C. Evolution of catalases from bacteria to humans. Antioxid Redox Signal. 2008;10(9):1527–48.
44. Meng L, Cheng Y, Tong X, Gan S, Ding Y, Zhang Y, Wang C, Xu L, Zhu Y, Wu J, Hu Y, Yuan A. Tumor oxygenation and hypoxia inducible Factor-1 functional Inhibition via a reactive oxygen species responsive nanoplatform for enhancing radiation therapy and abscopal effects. ACS Nano. 2018;12(8):8308–22.
45. Sivandzade F, Bhalerao A, Cucullo L. Analysis of the mitochondrial membrane potential using the cationic JC-1 dye as a sensitive fluorescent probe. Bio-protocol. 2019;9(1):e3128.
46. Zhang Z, Liu X, Chen D, Yu J. Radiotherapy combined with immunotherapy: the dawn of cancer treatment. Signal Transduct Target Therapy. 2022;7(1):258.
47. Wu T, Liu Y, Cao Y, Liu Z. Engineering macrophage exosome disguised biodegradable nanoplatform for enhanced sonodynamic therapy of glioblastoma. Adv Mater. 2022;34(15):e2110364.

Publisher's note